AMERICAN
METEOROLOGICAL
SOCIETY

Journal of Physical Oceanography

EARLY ONLINE RELEASE

This is a preliminary PDF of the author-produced manuscript that has been peer-reviewed and accepted for publication. Since it is being posted so soon after acceptance, it has not yet been copyedited, formatted, or processed by AMS Publications. This preliminary version of the manuscript may be downloaded, distributed, and cited, but please be aware that there will be visual differences and possibly some content differences between this version and the final published version.

The DOI for this manuscript is doi: 10.1175/2008JPO4025.1

The final published version of this manuscript will replace the preliminary version at the above DOI once it is available.

© 2008 American Meteorological Society

AMERICAN METEOROLOGICAL SOCIETY 1919

A new climatology of air-sea density fluxes and surface water mass transformation rates constrained by WOCE.

Nicola Howe

Arnaud Czaja

Department of Physics, Imperial College, London*

November 17, 2008

PRELIMINARY ACCEPTED VERSION

* Author address: Miss N. Howe, Imperial College, Prince Consort Road, Huxley Building, London SW7 2AZ, UK. email: n.howe06@imperial.ac.uk

Abstract

Global air-sea heat and freshwater flux data, constrained by WOCE hydrographic section transports, is used to construct a new global density flux climatology. Global transformations calculated using this density flux dataset show two regimes; surface waters with density less than ~ 23.3 kg m^{-3} are transformed to lighter density classes with a maximum rate of 130 Sv at $\sigma \sim 21.6$ kg m^{-3}; surface waters with density greater than 23.3 kg m^{-3} are transformed to denser density classes with a maximum rate of 100 Sv at $\sigma = 25.4$ kg m^{-3}. At higher density, ($\sigma = 27$ kg m^{-3}) the net transformation rates vanish reflecting heat loss in the Northern Hemisphere balanced by Southern Hemisphere freshening. This results in a kink in the global transformation rate, which we suggest is due to the presence of Drake Passage. Further analysis of the control run of the third Hadley Centre global climate model, HadCM3 suggests this feature to be robust and simply reflecting the "channel" geometry of the Southern Ocean and the "basin" geometry of the Northern Hemisphere.

1. Introduction

The density flux at the sea surface (D_{IN}) is calculated from the net heat flux into the ocean (Q_{net}) and the freshwater flux out of the ocean, evaporation (E) minus precipitation (P). It is given by

$$D_{IN} = \frac{-\alpha Q_{net}}{C_p} + \beta S(E - P)$$

where $\alpha = -1/\rho(\partial\rho/\partial T)$ and $\beta = 1/\rho(\partial\rho/\partial S)$ are the thermal and haline expansion coefficients respectively, C*p* is the specific heat, S and T are the sea surface salinity and temperature respectively. Past studies into air-sea density fluxes and associated transformation rates, using COADS, have produced differing results. Over the subtropical North Atlantic, for example Schmitt et al. (1989) found a weakly negative density flux that is confirmed by Large and Nurser (2001). However Speer et al. (1995) published a map of global (north of 30°S) annual density flux which shows the subtropical North Atlantic to be weakly gaining density. Previous observational air-sea density flux estimates have been limited by a lack of globally reliable heat and freshwater flux data. The advent of WOCE (World Ocean Circulation Experiment) has provided a tool with which to increase our confidence in heat and freshwater flux datasets over the ocean on a global scale. To calculate the air-sea fluxes we use a version of the National Oceanography Centre (NOC) global heat flux dataset constrained by 10 WOCE hydrographic section heat transports (Grist and Josey, 2003). In this study we complement this by comparing our freshwater flux dataset with 12 WOCE hydrographic freshwater transports (Ganachaud and Wunsch, 2003). Combining the heat and freshwater fluxes provides a new climatology of approximately balanced global air-sea density fluxes, which we will use to calculate a global surface water mass transformation rate.

The transformation rate is the volume flux of surface waters across outcropping isopycnals due to air-sea fluxes (Tziperman and Speer 1994). This is a useful diagnostic that can be used to calculate the rate of increase or decrease in volume of any density class at the surface. Walin (1982) first developed the approach used here to calculate transformation rates by making a connection between the cross isothermal flow and surface heat fluxes. Tziperman (1986) and Speer and Tziperman (1992) then made further connections between cross isopycnal flow and air-sea density fluxes. The air-sea density flux is summed over the area of the isopycnal outcrop and annually averaged following the seasonal migration of isopycnals over the ocean surface;

$$F(\rho) = \lim_{\Delta\rho \to 0} \frac{1}{\Delta\rho} \left(\frac{1}{1yr} \int_{year} dt \int_{outcrop\rho}^{outcrop\rho+\Delta\rho} D_{IN} dA \right)$$

For a detailed derivation of the water mass transformation rate see Tziperman (1986), Nurser et al. (1999) and Large and Nurser (2001). The difference between the flux of water entering and leaving a density range gives the volume of water formed in that density range. In a steady state ocean there is no net annual mean gain or loss of water mass at any particular density class. Assuming the real ocean is in steady state, a global increase in volume of a particular density class due to air-sea fluxes must be balanced by interior mixing. This is a powerful relationship that has been invoked in previous studies to link air-sea fluxes to interior ocean dynamics (Tziperman, 1986; Tziperman and Speer, 1994; Speer, 1997).

In section 2 we discuss the heat and freshwater datasets chosen to calculate the density flux and the WOCE section transport constraints applied. For readers more interested in the results of this study than the finer details of the dataset construction

we advise proceeding straight to section 3. Global maps of annual mean total density flux, plus the thermal and haline contributions to density flux, calculated by setting β or α to zero respectively, are presented in section 3. Comparisons are made with density fluxes calculated previously from observations by Schmitt et al. (1989), Speer et al. (1995) and Large and Nurser (2001).

The surface transformation rates presented in section 4 show the total transformation with the thermal and haline contributions, globally and for the Northern and Southern Hemispheres. We investigate the seasonal cycles of transformation over the whole surface density range, showing that the seasonality in density flux is driven by the heat fluxes, and compare estimates from our transformation rates of selected mode water formation rates to previously published values. Comparisons are made with previous observational transformation rates and a coupled climate model (HadCM3). Good agreement in overall shape and magnitude is found between our global transformation curve, the model and that calculated by Speer et al. (1995) using revised COADS data. We find a robust shape to our global transformation curve which is replicated by the model, namely a general cosine curve shape with a kink at high density. Density gain due to cooling in the observational dataset Northern Hemisphere is roughly balanced by density loss in the Southern Hemisphere due to precipitation. This kink occurs over density classes with outcropping isopycnals confined to the North Atlantic in the Northern Hemisphere and following a circuit through Drake Passage in the Southern Hemisphere, in both the observations and the model. The geographical similarities suggest that similar dynamics are controlling this feature in both. In section 5 a brief discussion of the uncertainties associated with the

density flux dataset and the sensitivity of the transformation rates to such errors is presented. The conclusions of this study are proposed in section 6.

2. Heat and freshwater flux datasets

a) Net Heat Flux

Grist and Josey (2003), henceforth GJ, produced three inverse analysis adjusted versions of the Southampton Oceanography Centre (NOC1.1) heat flux climatology using ten hydrographic estimates of ocean heat transport, taken from the World Ocean Circulation Experiment (WOCE) as constraints. NOC1.1 was constructed using ship meteorological reports, from the Comprehensive Ocean- Atmosphere Data Set 1a over the period 1980-93 (Josey et al. 1998 give a full account of the development of this climatology). The heat fluxes were calculated from the ship reports using semi-empirical formulas. The net heat flux (Q_{net}) between ocean and atmosphere, (positive values indicate ocean heat gain), is given by the linear combination of: incoming shortwave solar radiation (Q_{SW}); outgoing longwave radiation (Q_{LW}); upward sensible heat flux (Q_{SEN}) and; latent heat flux (Q_{LAT}).

GJ used adjustable parameters, as coefficients on the original climatology estimates of air-sea heat fluxes, to improve the agreement between the climatological and hydrographic estimates. They produced three solutions using this method. In solution 1, only the ten hydrographic constraints were applied and a global mean net heat loss of 5 W m^{-2} was achieved. In solution 2 they added the requirement of exact closure of the global ocean heat budget, i.e. to 0 W m^{-2}. GJ report that requiring exact closure results in an unacceptably large change to the latent heat flux. We have used the third solution in this study for which the added requirement was that the global mean net

heat flux is constrained to within ±2 W m^{-2} of global heat balance. Solution 3 has 22 W m^{-2} more global mean net cooling from increased sensible heat, latent heat and longwave radiation fluxes and 10 W m^{-2} less global mean net heating from decreased shortwave radiation flux compared with the original climatology. This adjusts the global mean net heat flux from 30 W m^{-2} to -2 W m^{-2}.

We have calculated the annual mean total Q_{net} between two hydrographic sections and compared these values to the heat transport divergences estimated by Ganachaud and Wunsch (2003), henceforth GW, for the same sections. The results plotted in Figure 1 show that the calculated values of total Q_{net} are well within the error bars of the transport divergences, (see Table 1 for the heat flux values). This is to be expected as these hydrographic sections were used as constraints in the inverse analysis carried out in GJ. We have also shown the contributions to Q_{net} for each section. The incoming shortwave radiation (always the greatest contribution) is offset mostly by the latent heat with a smaller contribution coming from the outgoing longwave radiation. The sensible heat values are much smaller than the other contributions everywhere.

GJ's solution 3 dataset contains no data for the Arctic Ocean, only reaching as far north in the Pacific Ocean as ~65°N and ~75°N in the Atlantic Ocean. In the Southern Ocean the solution 3 heat flux data extends to as far south as ~65°S in the Pacific Ocean section and ~55°S in the Atlantic Ocean section. This sparseness of data in the polar regions is a limitation on this study where we are attempting to produce a global density flux. Figure 2 is a global map of the annual mean position of isopycnal outcrops, calculated using salinity and temperature data from WOA2001. Figure 3

shows the percentage of each isopycnal outcrop (bin width $\Delta\rho = 0.1$ kg m^{-3}) for which values of Q_{net} are available and the average annual mean latitude following seasonal migrations of that isopycnal. This chart reflects the annual average global extent of Q_{net} with over 90% of isopycnal outcrops of density less than 1027 kg m^{-3} (all subsequent density values will be expressed as density anomalies, $\sigma = \rho$-1000 kg m^{-3}) covered by Q_{net} globally. For isopycnal outcrops of higher density anomaly the percentage rapidly drops off and the latitude ranges (shown in Figure 3 by the vertical bars) reach maximums of 75°S and 60°N. A comparison with the global map of isopycnal outcrop positions confirms that deviations from 100% global coverage of isopycnals by Q_{net} are caused by missing values at high latitudes. In section 4 we make comparisons to the HadCM3 control run which has global coverage and find that although we are not able to calculate the density flux for the highest density classes ($\sigma > 28$) with reliability, our geographical cover of the remaining surface density range is adequate.

b) Net Freshwater Flux

The global freshwater budget is a balance of precipitation (P), river runoff (R) and sea-ice melt (I_M) adding freshwater to the ocean and evaporation (E) plus sea-ice formation (I_F) removing it.

The evaporation dataset is calculated from the latent heat flux estimates of GJ using the following formula;

$$E = \frac{Q_{LAT}}{l_v}$$

where $l_v = 2.5\times10^6$ J kg^{-1} is latent heat of vaporisation. As the evaporation is calculated using the adjusted GJ latent heat flux dataset, we can be confident that no

further adjustment is necessary. To find global freshwater balance we consider adjustment to the contributors of freshwater to the system, namely precipitation, runoff and ice-melt and employ a strategy that uses the same constraint as GJ, namely the WOCE hydrographic sections.

For the freshwater input we used the National Center for Environmental Prediction, National Oceanic and Atmospheric Administration, Climate Prediction Center (NCEP-NOAA CPC) merged analysis of global monthly precipitation interpolated from a 2.5°×2.5° to a 1°×1° grid (Xie and Arkin 1996) and the four estimates of continental runoff compiled by Dai and Trenberth (2002). The aim of the CPC merged analysis was to combine estimates of precipitation from different sources in order to develop a global monthly precipitation dataset with an improved quality over the individual sources. They achieve this by employing a two step strategy. First the random error is reduced by combining satellite estimates (based on infra-red, microwave-scattering and microwave emission observational data) linearly with predictions from a numerical weather forecasting model. The second step was to blend the satellite and model analysis with gauge observations to reduce the systematic errors. For detailed information on the individual sources used and the analysis method, see Xie and Arkin (1996).

Dai and Trenberth (2002) compiled and compared four estimates of continental runoff: Fekete et al. (2002); 921 rivers; ECMWF; and NCEP. The annual mean estimate at one degree resolution using streamflow data from 921 of the world's largest rivers, although suffering from uncertainties (i.e. due to the use of estimates for discharge from the unmonitored areas, adjustments for river mouth flow rates,

inconsistent lengths and periods of streamflow records plus the effects of human influences), is likely to be closest to the truth according to Dai and Trenberth. We therefore use this dataset for runoff R in our climatology. The 921 Rivers dataset includes estimates by Jacobs et al. (1992) of the freshwater flux from Antarctica, which includes ice-shelf melting and runoff but not sea-ice.

As we are unaware of any accepted estimates for the total annual mean sea ice-melt in the Southern Ocean we have considered sea-ice concentrations from NASA's International Satellite Land Surface Climatology Project (ISLSCP) intended for use in Land-Atmosphere Models. This data is presented as monthly values of sea-ice concentration as a fraction of grid cell area for the period January 1987 to December 1988. Assuming the ice to be everywhere 1m thick a rough estimate of the amount of ice formed or melted annually over each grid cell can be calculated. We found that globally the annual total sea-ice melt almost exactly balances the annual total sea-ice formation. In the Southern Ocean we found the annual average sea-ice formation and melting rates were 0.4 Sv whereas in the Arctic Ocean (including North Pacific and Atlantic values) we calculated annual average formation and melting rates of 0.3 Sv. In comparison, the total annual global 921 rivers runoff calculated by Dai and Trenberth is 1.2 Sv. We have concluded from this that we can safely ignore the effects of sea ice-melt for this study however, as and when improved estimates of sea-ice become available it will be worth re-assessing this analysis.

The net air-sea freshwater exchanges presented by GW were derived from freshwater divergences, estimated using a geostrophic inverse model with hydrographic sections from WOCE. Figure 4 and Table 2 compare the freshwater flux estimates obtained by

GW, including associated errors, with those calculated using E, P and the 921 rivers dataset runoff values over the Atlantic, Pacific and Indian Oceans each separated into three regions. Precipitation and evaporation separately are everywhere greater than runoff. In the northern (47°N – 24°N) and tropical (24°N – 17°S) Pacific our study shows a small excess of evaporation over precipitation of a similar magnitude to the net runoff bringing P-E+R close to balance in these regions which is within the error bars of the GW estimate. In the southern (17°S – 30°S) Pacific, R is negligible (less than 0.01 Sv) and our estimates match GW almost exactly with excess evaporation. Elsewhere in our study R is also negligibly small compared to P-E, except in the tropical (24°N – 19°S) Atlantic where it is approximately half the value of P-E. In all of the Atlantic sections our study estimates an excess of evaporation. This is also true of GW tropical and southern (19°S – 30°S) Atlantic. The northern (47°N – 24°N) Atlantic is the only region in which our value is outside the GW estimate error bars. The estimates in our Indian Ocean sections have the same magnitude and sign as GW values but are always slightly more positive. Both estimates show excess precipitation in the tropical northern (North – 8°S) Indian versus excess evaporation in the tropical southern (8°S – 20°S) and southern (20°S – 32°S) Indian. If the Pacific and Indian Oceans are taken together, the total GW estimate is -0.64 ± 0.62 Sv compared to -0.64 Sv for our study, showing that overall our estimates for these two ocean basins are reliable with respect to GW. The dataset of P-E+R is globally (47°N – 30°S) net evaporative (excluding the Mediterranean Sea) with a value of -1.33 Sv which is comparable to the value reported by GW for the same latitude range of -1.2 ± 0.5 Sv.

The estimates of GW are employed here as constraints to the freshwater flux datasets previously described. In using the WOCE hydrographic sections as constraints, we

believe any adjustments required will be consistent with the adjustments made to the heat flux components of the NOC1.1 heat flux climatology by GJ. For consistency with GJ a constant adjustment (λ) to the precipitation dataset such that the freshwater flux (positive into the ocean) becomes λP-E+R is considered. As previously stated no adjustment is made to evaporation as this is derived from the already adjusted latent heat flux of GJ. The value of λ was determined by minimising the residual error between the adjusted freshwater flux and the GW estimates. When the Atlantic, Pacific and Indian basins are all included, the residual error reduces by 1% and the value of λ for which the residual has been minimised is 1.05. We note that in this analysis we have strived to remain consistent with GJ, where globally fixed parameter adjustments were used in the inverse analysis. Applying the globally fixed freshwater flux adjustment $\lambda = 1.05$ to P-E+R over all the ocean regions, results in small changes basin-wise. The tropical Pacific experiences the greatest change (of less than 0.2×10^9 kg s^{-1}) becoming an area of net precipitation instead of in balance. Therefore, it is reasonable to conclude that using the unadjusted precipitation values, i.e. $\lambda = 1$, is adequate for this study. A more detailed consideration of λ and the sensitivity of transformation rates to an adjustment on precipitation is discussed in section 5.

3. Surface Density Flux

The annual average density flux, D_{IN} is presented in Figure 5a. The contributions of thermal flux, Q_{IN}, and haline flux, H_{IN}, to the total density flux found by setting β or α to zero respectively are presented in Figure 5b/c. The contribution of thermal flux is greater in magnitude generally than the contribution of haline flux. The strongest positive signals in D_{IN} are the maximums over the Kurushio Current (10 mg m^{-2} s^{-1}), the Gulf Stream (12 mg m^{-2} s^{-1}) and the Agulhas Current (8 mg m^{-2} s^{-1}) corresponding

to strong cooling evident in Q_{IN}. The strongest negative signals in D_{IN} occur over the equatorial region (-6 mg m^{-2} s^{-1}) corresponding to strong heating, also evident in Q_{IN}.

a) North Atlantic

Schmitt et al. (1989) calculated the annual mean density flux plus haline and thermal contributions over the North Atlantic Ocean using heat flux estimates from Bunker (1976) and the precipitation estimates of Dorman and Bourke (1981). The density flux ($D_{Schmitt}$) presented by Schmitt et al. (1989) has a positive maximum of 14 mg m^{-2} s^{-1} over the Gulf Stream, which is 2 mg m^{-2} s^{-1} larger than the maximum in D_{IN}. D_{IN} is weakly positive over the subtropical North Atlantic whereas $D_{Schmitt}$ is weakly negative. An examination of the thermal ($Q_{Schmitt}$) and haline ($H_{Schmitt}$) contributions shows that the difference in the subtropics of $D_{Schmitt}$ and D_{IN} are caused by the thermal contributions. $H_{Schmitt}$ and H_{IN} have the same patterns in the North Atlantic subtropics but below a diagonal line from 20°N to 60°N $Q_{Schmitt}$ is negative (excess heating) whereas Q_{IN} is positive.

Global maps of average net heat and freshwater fluxes calculated for the period 1991-1993 and the resultant average density flux are presented by Large and Nurser (2001), henceforth LN. The heat fluxes used by LN were calculated with bulk formulae and a combination of satellite data, reanalysis data and ship and buoy data. For their freshwater flux (P-E) dataset they have blended the precipitation estimates of Xie and Arkin (1996) (also used in our climatology) with microwave sounding unit data used primarily in the tropical Indian and Pacific Oceans. LN found weak density loss in the subtropical North Atlantic on the same order of magnitude as in $D_{Schmitt}$. The patterns in LN freshwater flux over the North Atlantic are similar to the freshwater flux used

in our study whereas the net surface heat flux given by LN shows excess heating over the subtropical region with respect to GJ solution 3 heat fluxes.

We can explain the change in sign of D_{IN} over the subtropical North Atlantic compared with $D_{Schmitt}$ and LN estimates as due to the increase in latent cooling created by the inverse analysis adjustment to the NOC heat fluxes. The global (45°S - 70°N) revised COADS annual density flux (monthly means of COADS statistically revised) calculated by Speer et al. (1995), henceforth SIB shows the same patterns as our D_{IN} in the North Atlantic. The maximum density flux over the Gulf Stream of 16 mg m^{-2} s^{-1} is 4 mg m^{-2} s^{-1} greater than the maximum in $D_{IN.}$ SIB explain their difference in values of density flux over North Atlantic subtropics compared with estimates using the unrevised COADS and other datasets as due to an increase in evaporation introduced by the revision.

b) North Pacific

Cooling over the Kuroshio Current estimated by LN is of the order -125 W m^{-2}, the corresponding estimate given by Q_{net} is -150 W m^{-2}. The maximum D_{IN} over this region of 10 mg m^{-2} s^{-1} is 4 mg m^{-2} s^{-1} greater than the density flux estimated by LN and 2 mg m^{-2} s^{-1} greater than the maximum estimated by SIB using the revised COADS data. The pattern of positive and negative values of density flux in the North Pacific found in our study matches the SIB estimate well, however over the eastern subtropical North Pacific, LN found net density loss instead of the net density gain found in our study. Comparisons between the contributions to LN's density flux and the dataset presented here suggest that this deviation in the North Pacific is due to

increased latent heat/evaporation due to the inverse analysis performed on the heat fluxes.

c) Tropical

Intense heating over the equatorial eastern Pacific on the order of 100 W m^{-2} occurs in both Qnet and LN net heat flux estimates. The maximum in density loss due to the heating in this region in LN is on the order of 8 mg m^{-2} s^{-1}, the corresponding maximum density loss in D_{IN} is 6 mg m^{-2} s^{-1} and the SIB estimate has 8 mg m^{-2} s^{-1}. In LN there is an annual excess of evaporation between Borneo and the Philippines which is not evident in our estimate but despite this the overall pattern of equatorial density loss is the same for all three estimates.

d) Southern Ocean

In the Southern Ocean (south of 30°S) LN density flux is dominated by density loss with isolated density gain over the Agulhas Current and the southern-most western boundaries of the Atlantic, Pacific and Indian Oceans. D_{IN} is also dominated by density loss in the Southern Ocean but with larger density gains associated with the western boundaries. This difference can again be explained by the adjustments to the heat flux climatology which has resulted in increased heat loss over the Southern Hemisphere.

4. Results

a) Surface Water Mass Transformation

The annual global transformation rates due to air-sea fluxes ($F(\rho)$) as a function of density (bin width 0.1 kg m^{-3}) are presented in Figure 6a (solid line). Positive values

indicate transformation to denser water mass, i.e. globally surface waters with density $\sigma = 26$ are transformed to denser waters at a rate of 66 Sv. The amount of water mass produced over a year at a particular density class is the formation rate ($M(\rho)$) and is calculated from the negative gradients of the transformation curve. On this basis the global transformation curve shown in Figure 6a has three distinct regions. In the first region, $\sigma < 21.6$, $F(\rho)$ is negative, i.e. waters are transformed to a lighter density class. From Figure 2, showing the annual mean isopycnal outcropping positions, we can tell that these waters are equatorial. The formation rate of waters in this range is 130 Sv. The middle section covers the range $21.6 < \sigma < 25.4$ in which the transformation curve crosses zero at $\sigma \sim 23.3$. The gradient of $F(\rho)$ is positive in this section and there is net destruction globally of waters in this density range at a rate of 230 Sv. In the third section, $\sigma > 25.4$, $F(\rho)$ is positive, i.e. waters are transformed to a higher density class. There is an interesting feature in the transformation curve in this region. The transformation rate has a maxima at $\sigma = 25.4$, a local minima at $\sigma = 27$ (with $F(\rho)$ approximately equal to zero) and a secondary maxima at $\sigma = 27.3$ resulting in a kink in the transformation curve (which will be further discussed below). In terms of formation we can further divide this positive transformation region into three subsections. Global surface waters in the density ranges $25.4 < \sigma < 27$ and $\sigma > 27.3$ are formed at rates of 100 and 32 Sv respectively. Waters in the density class $27 < \sigma < 27.3$ are destroyed by air-sea fluxes globally at a rate of 32 Sv. This destruction of intermediate density class water is confined to the Southern Ocean and agrees well with the isopycnal range suggested by Lumpkin and Speer, (2007) to take part in the shallow Deacon Cell (Speer et al, 2000a).

The overall interpretation of this transformation curve is that air-sea fluxes act globally to make light surface waters lighter and dense surface waters denser. This results in a destruction of mid-latitude, intermediate density classes at the surface. Under the constraint that there is no net production or destruction of any density class in a steady state ocean, it is assumed that mixing acts to reverse the effects of air-sea fluxes.

To explain these features of the transformation curve, the haline (dashed line) and thermal (dotted line) contributions and the Northern and Southern hemisphere transformation rates (Figure 6b/c respectively) are presented. The haline contribution acts to transform waters of intermediate density in the range $22.3 < \sigma < 26.5$ to denser waters. There is a negative haline transformation rate of lighter density waters ($\sigma <$ 22.3) and denser waters ($\sigma > 26.5$). The total transformation rate more closely follows the thermal contribution, which has negative transformation over light surface waters $\sigma < 24$ and positive transformation over denser surface waters $\sigma > 24$. At $\sigma = 23.3$ where $F(\rho) = 0$, there is compensation between positive haline (due to excess evaporation) and negative thermal (due to excess heating) contributions in both hemispheres. The transformation rate over the Northern Hemisphere is dominated by the thermal contribution at high density. At $\sigma = 27$, where $F(\rho) \sim 0$ the haline contribution becomes less than 1 Sv and the thermal contribution, which is 15 Sv is nearly balanced by the combination of haline (-12 Sv) and thermal (-1 Sv) contributions in the Southern Hemisphere. Figure 2 shows that the $\sigma = 27$ isopycnal is mostly confined annually to the North Atlantic basin in the Northern Hemisphere. In the Southern Hemisphere this isopycnal follows a circuit through Drake Passage and outcrops south of 40°S throughout the year. Whether the compensation found here (~

15 Sv) is simply fortuitous or not is unclear. It does suggest a scenario in which, in steady state, there is negligible net mixing across this isopycnal which becomes the boundary separating northward flowing warm surface waters from southward flowing cold deep waters. This situation is dependent on negligible net mixing across isopycnals in the thermocline. Previous cross-isopycnal mixing studies (e.g. Speer, 1997) argue that this is the case. The North/South compensation found appears to support the argument for the majority of NADW returning to the surface by upwelling along isopycnals in the Southern Ocean, (Toggweiler and Samuels, 1995; Döös and Coward, 1997; Gnanadesikan, 1999), although given the limitations of our dataset this water mass is not fully resolved. This scenario and its implications as a mechanism for maintaining the strength of the thermohaline circulation will be discussed in a subsequent paper.

The pronounced kink in the Southern Hemisphere transformation curve, occurring over the density of an isopycnal which outcrops in a continuous circuit in the Southern Ocean throughout all seasons, reflects the air-sea interactions and ocean dynamics that can occur over a channel as opposed to a region with land-sea contrasts. From an air-sea interactions point of view, the dense, cold water upwelling in the Southern Ocean acts to lower the sea surface temperature. Lower temperatures result in reduced evaporation rates allowing precipitation to become dominant in the freshwater balance and creating buoyancy gain. This can be seen in the haline contribution to the Southern Hemisphere transformation rate. From a dynamical point of view, the westerly winds in the Southern Ocean drive equatorward Ekman transport. This transport (strictly speaking the "residual flow" at the surface, see Marshall and Radko, 2003) acts on a surface poleward density gradient so that parcels

of fluid crossing isopycnals must, in steady state, experience buoyancy gain. Thus both air-sea interaction and dynamical views predict negative transformation for isopycnals outcropping in Drake Passage. The compensation between this negative transformation and the positive transformation of dense waters in the Northern Hemisphere causes the kink in the total transformation curve. It will be shown in section 4 that this kink is a robust feature of the global transformation curve present also in several coupled climate models.

The revised COADS annual global (north of 30°S) transformation rate presented in SIB, as expected from the similarity in the global maps of air-sea density flux, shows the same basic features as the global $F(\rho)$ shown in Figure 6a. There is a net lightening of waters with $\sigma < 22.5$ and a net densification of waters with $\sigma > 22.5$. The maximum negative transformation of -90 Sv occurs near $\sigma = 21.5$ which corresponds with the maximum negative in $F(\rho)$ of -130 Sv at $\sigma = 21.6$. The maximum positive transformation in SIB is 80 Sv at $\sigma = 25$ whereas the maximum in $F(\rho)$ is 100 Sv occurring at $\sigma = 25.4$. The SIB density flux only covers the global ocean from 45°S - 70°N. The Southern Ocean south of 45°S in our climatology includes outcropping isopycnals $\sigma > 24$ experiencing mostly densification, so the greater maximum positive in $F(\rho)$ compared with SIB transformation is expected in this density range.

In contrast the transformation rates calculated by LN follow a different configuration to that shown by SIB and $F(\rho)$, (see Table 3). The transformation rates presented by LN (their Figure 5.1.14) are for the Arctic-Atlantic basin (excluding Mediterranean Sea), Indian-Pacific basin and the Southern Ocean separately. The Indian-Pacific basin and the Southern Ocean transformation rates are almost entirely negative with

minimums of approximately -100 Sv at σ = 22 and -55 Sv at σ = 27 respectively. The Arctic-Atlantic basin transformation rate is mostly negative with a minimum of -30 Sv at σ = 23.4 and a small positive transformation over isopycnals denser than σ = 26 with a maximum of 10 Sv at σ = 27.5. The implication in LN's transformation rates is that surface fluxes are acting everywhere to create lighter waters with the exception of the Northern Atlantic-Arctic Ocean where air-sea fluxes act to make surface waters denser. As Nurser et al. (1999) show, in an idealised ocean in steady state with zero net water mass formation of any density class, transformation is balanced by diffusion. As diffusion always acts to reduce the density contrast, we expect air-sea density fluxes to increase the density contrast. The surface-integrated density flux over all density classes in an idealised ocean in steady state should be zero, (ignoring the effects of cabbelling),

$$\frac{1}{1yr}\int\left(\int D_{IN}\,dxdy\right)dt = \int_{\rho\min}^{\rho\max} F(\rho)d\rho \approx 0$$

where ρ_{min} and ρ_{max} are the lightest and densest surface water density classes respectively. Integrating the transformation shown in Figure 6a over all densities results in a small deviation from zero (0.05×10^9 kg s^{-1}) but for the transformation curves presented by LN this is not true and we would expect a large negative deviation. This result emphasizes the importance of adjusting the heat and freshwater fluxes towards global balance.

b) Mode Water Formation Rates

Table 4 compares formation rates of selected mode waters calculated using the density flux climatology presented here with previous estimates. Speer and Tziperman (1992) used air-sea fluxes of heat and freshwater to calculate formation rates of North Atlantic Subtropical Mode Water (also known as 18° water, henceforth STMW). The

value quoted in Table 4, 12.6 Sv was estimated over the density range $26.2 < \sigma < 27$ from transformation rates calculated with a density bin width of 0.1 kg m^{-3}. Speer and Tziperman's best estimate for STMW taking bin width into account was 14 Sv which is still comparable to our estimate. They found two peaks in a calculation of mass source from density flux (their Figure 4), one centred over the density of STMW (σ = 26.5) and the other spanning densities within the ranges of North Atlantic Subpolar Mode Water (SPMW; $26.9 < \sigma < 27.75$) and Labrador Sea Water (LSW; $\sigma > 27.8$). A similar calculation using the air-sea density fluxes presented in section 2 shows very similar peaks centred over the same density classes (not shown). The SPMW formation rates shown in Table 4 were estimated over the density range $\sigma > 27.3$ as both datasets showed formation beginning at $\sigma = 27.3$ in the North Atlantic and continuing to the highest density class. As such these formation rates include formation of LSW. We estimate a formation rate of 12.7 Sv over the SPMW range of $27.3 < \sigma < 27.8$.

The estimate of Subantarctic Mode Water (SAMW) quoted for Speer et al (1997) is derived from their estimate of 25 Sv formed in the Indian Ocean sector which they claim is 65% of the total formation rate. Both estimates of SAMW formation rate are due to air-sea heat fluxes only for comparison purposes. We used the total transformation rate curve presented for the Southern Hemisphere in Figure 6c to estimate the SAMW formation rate of 29 Sv due to heat and freshwater air-sea fluxes.

c) Seasonality

The total, thermal and haline hemispheric monthly transformation rates are shown in Figure 7, Figure 8 and Figure 9 respectively. As Q_{IN} is generally a larger contribution

to D_{IN} than H_{IN} the total transformation rates follow the seasonal cycle of the thermal transformations. The monthly thermal transformation causes lightening over all outcropping isopycnals in both hemispheres in the summer months and densification over isopycnal outcrops denser than $\sigma = 22$ in winter months, (Figure 8). The monthly hemispheric haline transformation rates show very little or no seasonal changes, indicating that although the isopycnal outcrops migrate with the seasons, the amount of freshwater they gain or lose remains steady, (Figure 9). The reason for this, in the case of most isopycnals such as those in the range $21 < \sigma < 22$, is that the isopycnal remaining predominantly within a band of precipitation, i.e. the ITCZ, throughout the year. The effect of the ITCZ can be seen in the Northern and Southern Hemispheres with the boundary between negative (net precipitation) and positive (net evaporation) haline transformations generally between $22 < \sigma < 23$. The Northern Hemisphere outcrops above $\sigma = 22$ and the Southern Hemisphere outcrops between $23 < \sigma < 26$ experience mostly positive haline transformation throughout the year. In the Southern Hemisphere higher density classes $\sigma > 26$ experience negative haline transformation throughout the year. These features correspond with the annual mean transformation curves discussed previously.

d) Coupled Climate Model

We have compared the transformation rates calculated from our new climatology with transformation rates calculated from the third Hadley Centre coupled climate model (HadCM3) 100 year control run. HadCM3 does not require flux adjustments at the ocean-atmosphere interface. It has realistic surface heat fluxes and ocean poleward heat transports comparable to observed estimates. A description of HadCM3 is given by Gordon et al. (2000). The 100 year monthly mean climatology was used to

calculate transformation rates, shown in Figure 10. We have not included effects of sea-ice nor runoff in the freshwater flux but use instead only evaporation and precipitation, which is consistent with our observational method. The global transformation for the model control run (Figure 10a) shows similarities to the observational F(ρ) (Figure 6a), although the range of surface density extends to lighter classes ($\sigma < 19$) in the model. In direct comparison with the global observational F(ρ) the global HadCM3 control run F(ρ) can be divided into three main sections. Surface waters in the density range $\sigma < 22.6$ are formed at a rate of 52 Sv. Surface waters in the range $22.6 < \sigma < 24.4$ are destroyed at a rate of 103 Sv and $F(\rho) \sim 0$ at $\sigma = 23.4$. The third section shows the same feature as the third section of the observational transformation curve but more pronounced. The density range $24.4 < \sigma < 26.4$ is formed at a rate of 74 Sv. There is a negative transformation over the range $26.1 < \sigma < 26.7$ with a secondary minima at 26.4 of -23 Sv. Surface water in the density range $26.4 < \sigma < 27.2$ is destroyed at a rate of 44 Sv.

The magnitudes of the maximum and minimum model transformation rates are about a factor two lower than the corresponding values in the observational transformation curve. Comparisons between the model and observational global haline and thermal transformation curves can explain this reduction. The haline contribution (Figure 10a, dashed line) is the same order of magnitude as our observational haline contribution, with the same basic features of excess precipitation over low and high density classes and excess evaporation over intermediate density classes. However, the negative haline transformation over low densities in the model is spread over a wider density range, $18 < \sigma < 21.7$ compared with $20 < \sigma < 22.3$ in the observational dataset, and the minimum is shifted to lower density. At higher densities the model haline contribution

is more negative than the observational contribution. Extending this analysis over the Northern and Southern Hemispheres (Figure 10b/c), the model haline contributions are weaker and broader over low densities and of similar magnitude but shifted to lower density over the intermediate range in both cases compared with the observational contributions. We suggest that the causes of these differences in haline contributions are the double ITCZ present in the HadCM3 control run and the reduction in subtropical precipitation compared with the observational dataset of Xie and Arkin. As noted by Pardaens et al (2003) HadCM3 exhibits stronger precipitation than the observational dataset used in this study whereas we find the evaporation datasets are similar (not shown). In the Northern Hemisphere the haline contribution (Figure 10b, dashed line) does not drop to almost zero over higher density classes as the observational haline contribution does, but it is still a much smaller contribution to $F(\rho)$ than the thermal contribution over this density range. In the Southern Hemisphere the haline contribution (Figure 10c, dashed line) is negative over the higher density range as in the observational case, but the minimum value is -24 Sv at $\sigma = 26.5$ compared to the observational minimum of -12 Sv at $\sigma = 27$.

The model thermal contribution (Figure 10a, dotted line) over densities $\sigma < 24$ is negative as in the observational dataset and with the same order of magnitude. The thermal transformation minimum in the model is about -88 Sv at $\sigma = 22.6$ whereas the observational minimum is -92 Sv at $\sigma = 21.9$. These values suggest that the reason the minimum in the model $F(\rho)$ is over a factor two lower than the observational minimum is the shift in model contributions. The observational thermal and haline contribution minimums over the lower density range line up creating a large negative in $F(\rho)$. In contrast the model haline contribution minimum is shifted with respect to

the observations to lower densities and the thermal contribution is shifted to higher densities, resulting in a fairly constant $F(\rho) \sim 45$ Sv over the density range $20.5 < \sigma < 23$. This the greatest difference between the two total global transformation rates.

Over the density range $\sigma > 24$ the model and observational thermal contributions are no longer of similar magnitude. The model thermal contribution is on average a factor two lower than the observational contribution. In the model Southern Hemisphere the thermal contribution (Figure 10c, dotted line) has a maximum of 17 Sv compared to the observational maximum of 54 Sv. In the Northern Hemisphere larger thermal contributions (Figure 10b, dotted line) over the Kurushio Current and the Gulf Stream density ranges are seen in the observations, around 33 Sv at $\sigma \sim 25$ and 37 Sv at $\sigma \sim 26$, whereas the model thermal contribution remains below 23 Sv. Although the model exhibits more intense cooling at the core of Western Boundary Currents in both hemispheres (not shown), the observational thermal flux (Figure 5b) is more extensively cooling over the subtropical basins resulting in a larger thermal contribution to $F(\rho)$.

The Southern Hemisphere observational thermal contribution at $\sigma = 27$ is close to zero. The corresponding model transformation curve has a local minimum of -15 Sv at $\sigma = 26.4$. Isopycnals in the range $26.3 < \sigma < 26.5$, have similar geographical positions as the observational dataset $\sigma = 27$ isopycnal (not shown) and are also uninterrupted by land in the Southern Ocean. For this reason we suspect similar dynamics in both the observations and the model result in the transformation kink seen. We note that a comparison with the Atlantic and Arctic and Southern Ocean transformation rates calculated for the non flux adjusted NCAR Climate System

Model (see Doney et al. 1998) adds encouragement to our results. There is a large negative transformation in the Southern Ocean over the density range $26 < \sigma < 27$ which is balanced by a positive transformation in the Arctic and Atlantic basin. Such compensation was also suggested solely from the consideration of heat budgets by Speer et al (2000b) with the OPA8-ARPEGE coupled model.

In a steady state idealised basin mixing will compensate the effects of air-sea density fluxes. Nurser et al. (1999) describe an idealised example of a closed basin in steady state. They reason that the air sea fluxes must be attempting to counteract the effects of mixing, i.e. acting to increase the density contrast. It is therefore suggested that the net density flux through the air-sea interface is positive over all densities peaking at some intermediate density and falling to zero at the minimum and maximum outcropping densities mirroring the diffusive flux which is always negative (see their Figure 5). The transformation rate given by this idealised density flux takes a cosine shape (Figure 11, solid line). If Drake Passage was closed we would expect the real ocean to behave similarly to an idealised closed steady state basin with a transformation curve closely resembling this hypothetical form. As this study has shown however, the presence of Drake Passage forces the transformation curve to deviate from the closed basin theory with a kink, shown in Figure 11 by the dashed line. The implications of this kink for the thermohaline circulation will be explored further elsewhere.

5. Discussions

Using GJ inverse analysis adjusted heat fluxes has led to an approximately balanced density flux dataset. The global ocean transformation rate is correspondingly also balanced as discussed in section 4. The sensitivity of the total transformation rate to changes in the heat flux can be explored by a comparison of the transformation rates produced in this study and those calculated using the original NOC dataset. The original NOC heat flux climatology produces a transformation rate which is almost entirely negative with a minimum value of ~ 260 Sv at σ = 21.8 (not shown). The result is a transformation rate which is not in balance implying that the ocean is gaining buoyancy everywhere except the Poles. GJ provided three solutions to the inverse analysis; the first uses only the 10 WOCE hydrographic heat transports resulting in a global mean net heat flux of -5 W m^{-2}; the second is as the first with the additional constraint that global mean net heat flux exactly balances to zero; the third is as the second but with the global mean net heat flux constrained to within ±2 W m^{-2} of global heat balance. Comparisons of transformation rates calculated for each solution (not shown) indicate that there are negligible differences. In this study we used the third solution which is, according to GJ, more consistent with observations of ocean temperature variations on a decadal timescale.

The inverse analysis adjustment method used by GJ involved adjustable parameters on each component which could be used to find the greatest agreement between the WOCE heat transport estimates and the values derived from the NOC climatology, in a least squares sense. We have used a simplified version of this method to constrain the freshwater fluxes. As evaporation is calculated from latent heat it has already been optimally adjusted and can be left as is. Transformations due to river runoff and sea-ice are localised effects and small enough to be ignored in this study (maximum

transformation due to runoff was found to be 8 Sv; transformation due to sea-ice peaked at 7 Sv). The other variable of freshwater flux that is used in calculating the density flux is precipitation so the adjustable parameter λ is applied to this component. The optimal value of λ is found by calculating the residual error between λP-E+R and GW freshwater fluxes for a range of λ using a Monte-Carlo approach.

It was found that setting $\lambda = 1.13$ reduces the residual error in the closed Atlantic basin (30°S - 47°N) by 18%. For the closed Pacific (30°S - 47°N) and Indian (32°S – North) ocean basins setting $\lambda = 1.06$ and 0.8 reduces the residual error by 8% and 3% respectively. Having taken into account the extent of missing values (due to limitations in evaporation, see Figure 3) for our freshwater flux in the polar ocean regions, the size of the Southern Ocean error estimated by GW and the uncertainties associated with sea-ice, we concluded that it is not meaningful to include the regions north of 47°N and south of 30°S in comparisons of the two freshwater exchange estimates. For the closed Pacific and Atlantic basins which are more evaporative in our dataset than the GW estimates, λ is required to be greater than 1, (1.13 and 1.06) and for the closed Indian basin λ is required to be less than 1, (0.8). The value of λ found to reduce the residual error the most is between these values. Calculations of the total transformation rate using this value, $\lambda = 1.05$ as an adjustment on precipitation deviate from those shown in Figure 6 by less than 0.5 Sv over most densities. To make a significant alteration to the transformation rate λ must be much greater, for example applying $\lambda = 0.5$ and 1.5 changes the global transformation rate by ~ 20 Sv.

Another source of errors is the lack of consideration in this study of the effects of mesoscale eddies. It is becoming possible to estimate from observations the eddy heat flux (Speer et al, 2008). This is also possible for the HadCM3 model (or one can go even further by adjusting the model physics as in the study of Speer et al, 2000b) in which the Visbeck et al (1997) (locally determined coefficient) version of the Gent and McWilliams (1990) adiabatic diffusion scheme is used to parameterise sub-grid scale eddy activity. It is particularly important over the Southern Ocean to take into account the effects of eddies as they are believed to play a significant role in the meridional circulation by transporting mass southward as a neccessary part of the Deacon cell, (Olbers et al, 2001; Speer et al, 2000a). This task is however, beyond the scope of this paper which was to constrain the large scale budgets using WOCE.

In section 4d transformation rates calculated from the monthly mean climatology of the 100 year control run of HadCM3 were compared to the observational results. In order to investigate the variability of the transformation curve over time decadal monthly climatologies were produced from which a timeseries of transformation rates could be calculated. It was found that the main features of the transformation rate are present in all decadal transformation rates. The kink at densities outcropping through Drake Passage is confirmed as a robust feature with small variations in density over which the minimum point occurs corresponding to changes in the Southern Ocean density field. An indication of the variability is given by the standard deviation from the mean of the decadal transformations (not shown). Over the majority of densities one standard deviation is ~ 5 Sv. The variability is smaller for higher density classes ($\sigma > 26$).

6. Conclusions

We have presented a new global density flux climatology based on an inverse analysis adjusted NOC heat flux dataset, with closure of the heat budget to -2 W m^{-2}. We employed a strategy consistent with the adjustments made by GJ to the NOC heat fluxes by constraining the freshwater flux with WOCE hydrographic freshwater transports. Our annual mean global density flux climatology gives more confidence to the density flux presented by Speer et al. (1995) using revised COADS than that of Large and Nurser (2001) in certain oceanic regions, specifically the subtropical North Atlantic. The adjustments to the latent heat flux made by GJ are responsible for an increased positive density flux over the North Atlantic which contributes to our resultant total transformation rate integrated over all density classes approaching zero.

Surface water mass transformation rates calculated using this new climatology for the global ocean show formation of light waters $\sigma < 21.6$ at a rate of 130 Sv and formation of dense waters $\sigma > 25.4$ at a rate of 100 Sv. Destruction of intermediate density waters is compensated for by creation due to mixing in the steady state. A balance of thermal and haline fluxes is found in the global surface transformation curve along the $\sigma = 27$ isopycnal, an isopycnal which goes through Drake Passage in the Southern Ocean. Further calculations of Northern and Southern Hemisphere transformation rates show that the balance along this isopycnal is caused by winter cooling in the North Atlantic and summer precipitation in the Southern Ocean. Support for this asymmetry between hemispheres is provided by several coupled models and as idealised in Figure 11 suggests a simple signature of Drake Passage in

global transformation rates. The air-sea density flux climatology used for this study of global transformation rates is freely available upon request from the authors.

Acknowledgements: Nicola Howe was funded by the Natural Environment Research Council. The authors would like to thank Jonathan Gregory for help and advice concerning the HadCM3 data.

References

Bunker, A., 1976: Computations of surface-energy flux and annual air-sea interaction cycles of North-Atlantic Ocean. *Monthly Weather Review,* **104,** 1122-1140.

Dai, A., and K. Trenberth, 2002: Estimates of freshwater discharge from continents: Latitudinal and seasonal variations. *Journal of Hydrometeorology,* **3,** 660-687.

Doney, S., W. Large, and F. Bryan, 1998: Surface ocean fluxes and water-mass transformation rates in the coupled NCAR Climate System Model. *Journal of Climate,* **11,** 1420-1441.

Doos, K., and A. Coward, 1997: The Southern Ocean as the major upwelling zone of North Atlantic Deep Water. *International WOCE Newsletter,* **27,** 3-4.

Dorman, C., and R. Bourke, 1981: Precipitation over the Atlantic-Ocean, 30°S to 70°N. *Monthly Weather Review,* **109,** 554-563.

Fekete, B., C. Vorosmarty, and W. Grabs, 2002: High-resolution fields of global runoff combining observed river discharge and simulated water balances. *Global Biogeochemical Cycles,* **16,** 1042-1057.

Ganachaud, A., and C. Wunsch, 2003: Large-scale ocean heat and freshwater transports during the World Ocean Circulation Experiment. *Journal of Climate,* **16,** 696-705.

Gent, P., and J. McWilliams, 1990: Isopycnal mixing in ocean circulation models. *Journal of Physical Oceanography,* **20,** 150-155.

Gnanadesikan, A., 1999: A simple predictive model for the structure of the oceanic pycnocline. *Science,* **283,** 2077-2079.

Gordon, C., C. Cooper, C. Senior, H. Banks, J. Gregory, T. Johns, et al., 2000: The simulation of SST, sea ice extents and ocean heat transports in a version of the Hadley Centre coupled model without flux adjustments. *Climate Dynamics,* **16,** 147-168.

Grist, J., S. Josey, 2003: Inverse analysis adjustment of the SOC air-sea flux climatology using ocean heat transport constraints. *Journal of Climate,* **16,** 3274-3295.

Jacobs, S., H. Helmer, C. Doake, A. Jenkins, and R. Frolich, 1992: Melting of ice shelves and the mass balance of Antarctica. *Journal of Glaciology,* **38,** 375-387.

Josey, S., E. Kent, and P. Taylor, 1998: The Southampton Oceanography Centre (SOC) ocean-atmosphere heat, momentum and freshwater flux atlas. *Southampton Oceanography Centre Report,* **No 6**.

Large, W., and A. Nurser, 2001: Ocean surface water mass transformation. *In:* Siedler, G., J. Church, and J. Gould, (Eds.): *Ocean Circulation and Climate:Observing and Modelling the Global Ocean,* **Academic Press,** pp. 317-336.

Lumpkin, R., and K. Speer, 2007: Global ocean meridional overturning. *Journal of Physical Oceanography,* **37,** 2550-2562.

Marshall, J., and T. Radko, 2003: Residual-mean solutions for the Antarctic Circumpolar Current and its associated overturning circulation. *Journal of Physical Oceanography,* **33,** 2341-2354.

Nurser, A., R. Marsh, and R. Williams, 1999: Diagnosing water mass formation from air-sea fluxes and surface mixing. *Journal of Physical Oceanography,* **29,** 1468-1487.

Pardaens, A., H. Banks, J. Gregory, and P. Rowntree, 2003: Freshwater transports in HadCM3. *Climate dynamics,* **21,** 177-195.

Rintoul, S., C. Hughes, and D. Olbers, 2001: The Antarctic Circumpolar current system. *In:* Siedler, G., J. Church, and J. Gould, (Eds.): *Ocean Circulation and Climate:Observing and Modelling the Global Ocean,* **Academic Press,** pp. 271-300.

Sallee, J., R. Morrow, and K. Speer, 2008: Eddy heat diffusion and subantarctic mode water formation. *Geophysical Research Letters,* **35,** L05607.

Schmitt, R., P. Bogden, and C. Dorman, 1989: Evaporation minus precipitation and density fluxes for the North-Atlantic. *Journal of Physical Oceanography,* **19,** 1208-1221.

Speer, K., and E. Tziperman, 1992: Rates of water mass formation in the North-Atlantic Ocean. *Journal of Physical Oceanography,* **22,** 93-104.

Speer, K., H. Isemer, and A. Biastoch, 1995: Water mass formation from revised Coads Data. *Journal of Physical Oceanography,* **25,** 2444-2457.

Speer, K., 1997: A note on average cross-isopycnal mixing in the North Atlantic Ocean. *Deep-sea research Part I,* **44,** 1981-1990.

Speer, K., S. Rintoul, and B. Sloyan, 1997: Subantarctic mode water formation by air-sea fluxes. *International WOCE newsletter,* **No 29,** 29-31.

Speer, K., S. Rintoul, B. Sloyan, 2000a: The diabatic Deacon Cell. *Journal of Physical Oceanography,* **30,** 3212-3222.

Speer, K., E. Guilyardi, and G. Madec, 2000b: Southern Ocean transformation in a coupled model with and without eddy mass fluxes. *Tellus Series A,* **52A,** 554-565.

Toggweiler, J., and B. Samuels, 1995: Effect of Drake Passage on the global thermohaline circulation. *Deep-Sea Research Part I,* **42,** 477-500.

Tziperman, E., 1986: On the role of interior mixing and air-sea fluxes in determining the stratification and circulation of the oceans. *Journal of Physical Oceanography,* **16,** 680-693.

Tziperman, E., and K. Speer, 1994: A study of water mass transformation in the Mediterranean-Sea - Analysis of climatological data and a simple 3-box model. *Dynamics of Atmospheres and Oceans,* **21,** 53-82.

Visbeck, M., J. Marshall, T. Haine, and M. Spall, 1997: Specification of eddy transfer coefficients in coarse-resolution ocean circulation models. *Journal of Physical Oceanography,* **27,** 381-402.

Walin, G., 1982: On the relation between sea-surface heat-flow and thermal circulation in the ocean. *Tellus,* **34,** 187-195.

Xie, P., and P. Arkin, 1996: Analyses of global monthly precipitation using gauge observations, satellite estimates, and numerical model predictions. *Journal of Climate,* **9(4),** 840-858.

7. List of Figures

Figure 1 Comparison of Ganachaud and Wunsch (2003) net heat flux and Grist and Josey (2003) solution 3 radiative, sensible, latent and net heat fluxes over the Atlantic Ocean, the Indo-Pacific Ocean and the Global Ocean (excluding the Mediterranean Sea) northern (47°N - 24°N) and tropical (24°N - 30°S) regions.

Figure 2 Annual mean global outcroppings of isopycnals calculated using WOA 2001 temperature and salinity values, ρ-1000 kg m^{-3}.

Figure 3 The annual mean extent of surface isopycnals from WOA 2001 covered by Grist and Josey (2003) solution 3 Qnet globally (white boxes) and over the Northern (gray boxes) and Southern Hemisphere (black and white striped boxes) as a percentage. On the second vertical axis the average latitude of isopycnals at the surface in the Northern (dashed line) and Southern (solid line) Hemispheres is plotted with vertical bars indicating the latitude range with the maximum and minimum latitudes.

Figure 4 Comparison of Ganachaud and Wunsch (2003) net freshwater flux against evaporation calculated from Grist and Josey (2003) solution 3, precipitation from Xie and Arkin (1996) and 921 rivers runoff estimate from Dai and Trenberth (2002). Atlantic Ocean regions from GW2003 are northern (47°N – 24°N), tropical (24°N – 19°S) and southern (19°S – 30°S). Indian Ocean regions are tropical northern (North – 8°S), tropical southern (8°S – 20°S) and southern (20°S – 32°S). Pacific regions are north (47°N – 24°N), tropical (24°N – 17°S) and southern (17°S – 30°S).

Figure 5 (a) Annual average global surface density flux, D_{IN} with contour intervals of 2mg m^{-2} s^{-1}, positive values thin black line, negative values are shaded. (b) Annual average global thermal contribution to surface density flux, Q_{IN} with contour interval 2mg m^{-2} s^{-1}. (c) Annual average global haline contribution to surface density flux, H_{IN} with contour interval 0.5mg m^3 s^{-1}.

Figure 6 (a) Global annual surface water mass transformation as a function of sea surface density divided into total transformation (solid line), thermal contribution (dotted line) and haline contribution (dashed line). (b) Northern Hemisphere. (c) Southern Hemisphere.

Figure 7 Northern/Southern Hemisphere monthly transformation rate, contour interval 50×10^6 m^3 s^{-1}, thick solid line is contour of zero transformation, negative values are shaded.

Figure 8 Northern/Southern Hemisphere monthly thermal transformation rate, contour interval 50×10^6 m^3 s^{-1}, thick solid line is contour of zero transformation, negative values are shaded.

Figure 9 Northern/Southern Hemisphere monthly haline transformation rate, contour interval 10×10^6 m^3 s^{-1}, thick solid line is contour of zero transformation, negative values are shaded.

Figure 10 (a) HadCM3 control run global annual surface water mass transformation as a function of sea surface density divided into total transformation, solid line,

thermal contribution, dotted line and haline contribution, dashed line. (b) Northern Hemisphere. (c) Southern Hemisphere.

Figure 11 Schematic of transformation curves over a range of densities from intermediate (ρ_{int}) to maximum (ρ_{max}), for an idealised steady state ocean with Drake Passage closed (solid line) and with Drake Passage open (dashed line), where ρ_{DP} is the density class with the outcropping isopycnal which circumnavigates the Southern Ocean uninterrupted by land.

Table 1 Comparisons of Ganachaud and Wunsch (2003) net heat flux in Wm^{-2} against Grist and Josey (2003) solution 3 radiative, sensible, latent and net heat fluxes.

Ocean	Latitudes	GW	GW Error	Incoming Shortwave	Outgoing Longwave	Latent	Sensible	Qnet
Atlantic	47N-24N	-0.5	0.1	2.5	-0.9	-1.9	-0.2	-0.5
Atlantic	24N-30S	0.7	0.2	6.7	-1.9	-4.2	-0.2	0.5
Indo-Pacific	47N-24N	-0.6	0.2	3.7	-1.4	-2.7	-0.3	-0.6
Indo-Pacific	24N-30S	1.6	0.4	26.3	-7.1	-17.3	-0.9	1.0
Total	47N-24N	-1.1	0.2	6.3	-2.3	-4.6	-0.5	-1.1
Total	24N-30S	2.3	0.4	33.0	-9.0	-21.5	-1.1	1.4

Table 2 Comparisons of Ganachaud and Wunsch (2003) net freshwater flux $\times 10^9$ kg s^{-1} against evaporation calculated from Grist and Josey (2003) solution 3 latent heat flux, precipitation from Xie and Arkin (1996) and 921 rivers runoff dataset from Dai and Trenberth (2002).

Ocean	Latitudes	GW	GW Error	Evaporation	Precipitation	Runoff	P-E+R
Atlantic	47N-24N	0	0.15	0.75	0.45	0.05	-0.25
	24N-19S	-0.1	0.2	1.55	0.83	0.43	-0.30
	19S-30S	-0.36	0.2	0.29	0.14	0.01	-0.15
Indian	North-8S	0.1	0.25	0.96	1.12	0.09	0.25
	8S-20S	-0.33	0.2	0.61	0.36	0.03	-0.22
	20S-32S	-0.35	0.3	0.52	0.16	0.03	-0.33
Pacific	47N-24N	0.14	0.26	0.96	0.82	0.08	-0.06
	24N-17S	0.1	0.3	4.21	4.09	0.13	0.002
	17S-30S	-0.3	0.2	0.80	0.52	0.002	-0.27

Table 3 Maximum and minimum transformation values from our study compared with the corresponding values estimated from the transformation curves presented by Speer at al. (1995) and Large and Nurser (2001) and that calculated for HadCM3 control run.

	Our Study		SIB		LN		HadCM3	
	F(ρ), Sv	Density anomaly, kg m^{-3}	F(ρ), Sv	Density anomaly, kg m^{-3}	F(ρ), Sv	Density anomaly, kg m^{-3}	F(ρ), Sv	Density anomaly, kg m^{-3}
Max	100	26	80	25	10	27.5	51	24.4
Min	-130	21.5	-90	21.5	-110	22	-50	22.6

Table 4 Comparisons of selected Mode Water formation rates estimated using the negative gradients of transformation curves calculated from the air-sea density flux climatology discussed in section 2, versus previously reported values. The SAMW values are estimates of formation due to air-sea heat fluxes only following the methodology of Speer et al, all other values are for the full air-sea density flux formation rates.

Water Mass	M(ρ), Sv	Previous estimate, Sv	Source
18° Water ($26.2 < \sigma < 27$)	11.5	12.6	Speer and Tziperman (1992)
SPMW + LSW ($\sigma > 27.3$)	21.4	16.7	Speer and Tziperman (1992)
SAMW (F_{heat}; $26.5 < \sigma < 27$)	20	38	Speer et al. (1997)

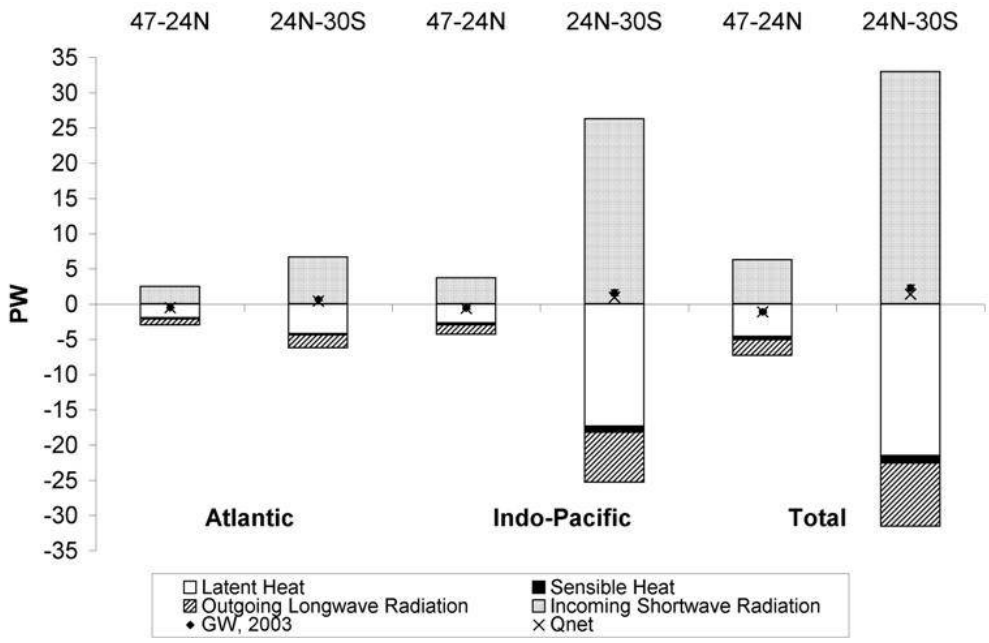

Figure 1 Comparison of Ganachaud and Wunsch (2003) net heat flux and Grist and Josey (2003) solution 3 radiative, sensible, latent and net heat fluxes over the Atlantic Ocean, the Indo-Pacific Ocean and the Global Ocean (excluding the Mediterranean Sea) northern (47°N - 24°N) and tropical (24°N - 30°S) regions.

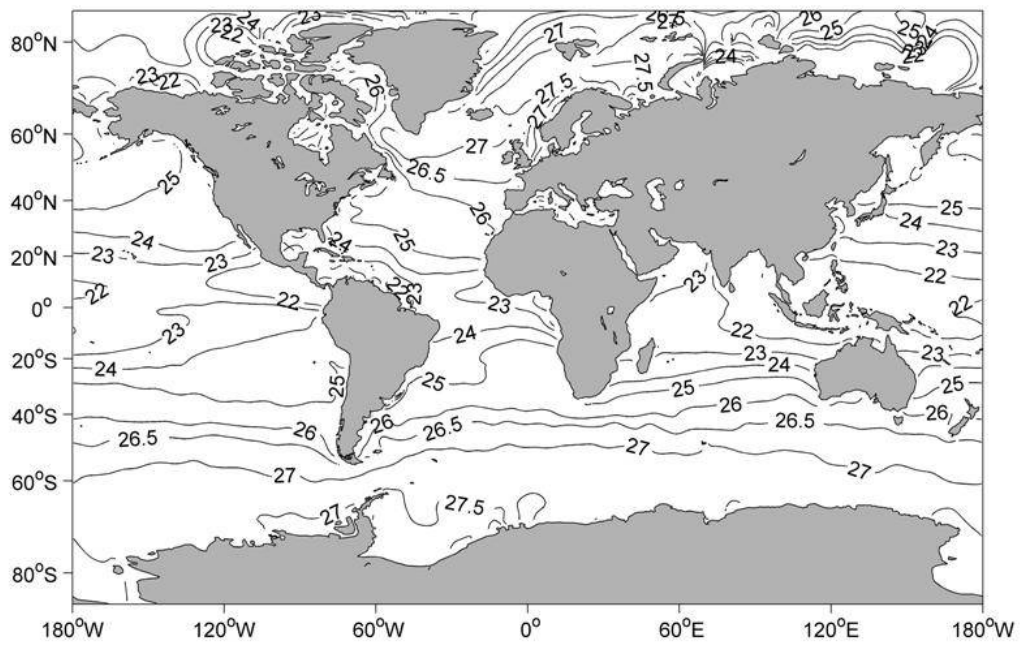

Figure 2 Annual mean global outcroppings of isopycnals calculated using WOA 2001 temperature and salinity values, ρ-1000 kg m^{-3}.

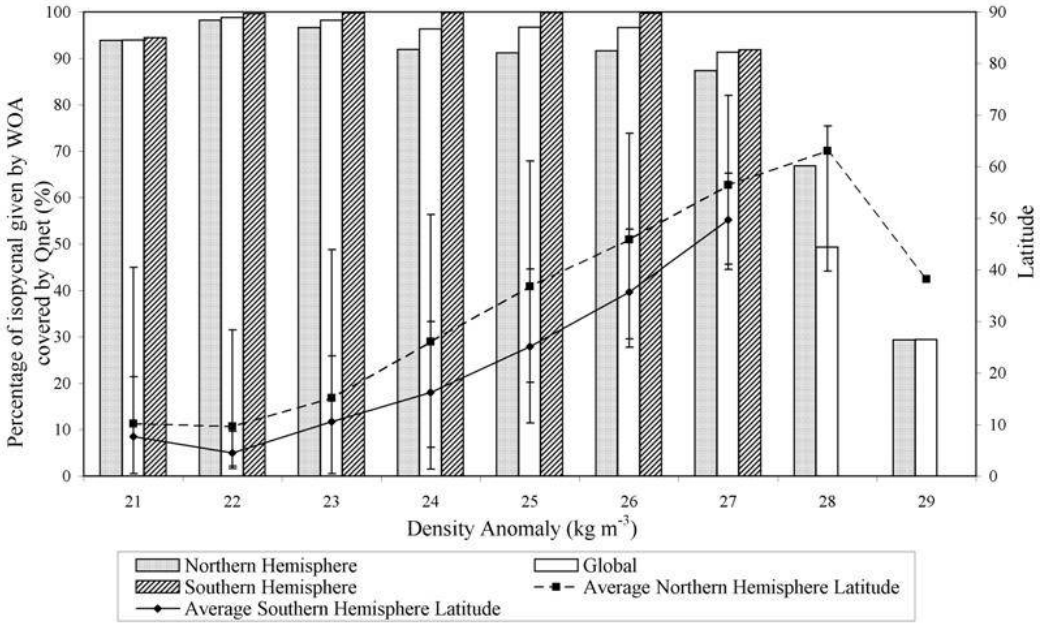

Figure 3 The annual mean extent of surface isopycnals from WOA 2001 covered by Grist and Josey (2003) solution 3 Qnet globally (white boxes) and over the Northern (gray boxes) and Southern Hemisphere (black and white striped boxes) as a percentage. On the second vertical axis the average latitude of isopycnals at the surface in the Northern (dashed line) and Southern (solid line) Hemispheres is plotted with vertical bars indicating the latitude range with the maximum and minimum latitudes.

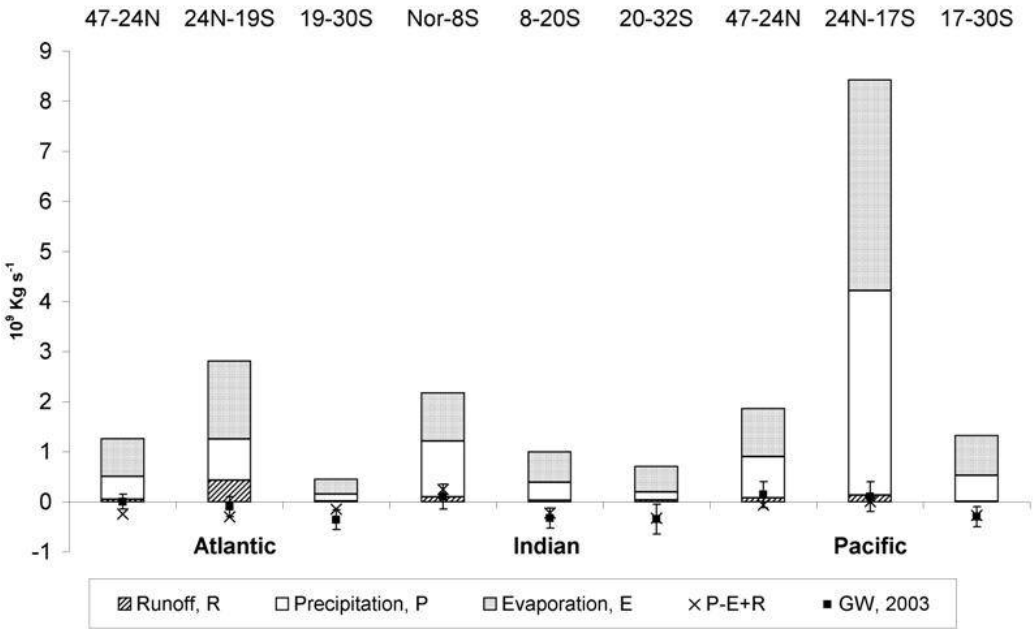

Figure 4 Comparison of Ganachaud and Wunsch (2003) net freshwater flux against evaporation calculated from Grist and Josey (2003) solution 3, precipitation from Xie and Arkin (1996) and 921 rivers runoff estimate from Dai and Trenberth (2002). Atlantic Ocean regions from GW2003 are northern (47°N – 24°N), tropical (24°N – 19°S) and southern (19°S – 30°S). Indian Ocean regions are tropical northern (North – 8°S), tropical southern (8°S – 20°S) and southern (20°S – 32°S). Pacific regions are north (47°N – 24°N), tropical (24°N – 17°S) and southern (17°S – 30°S).

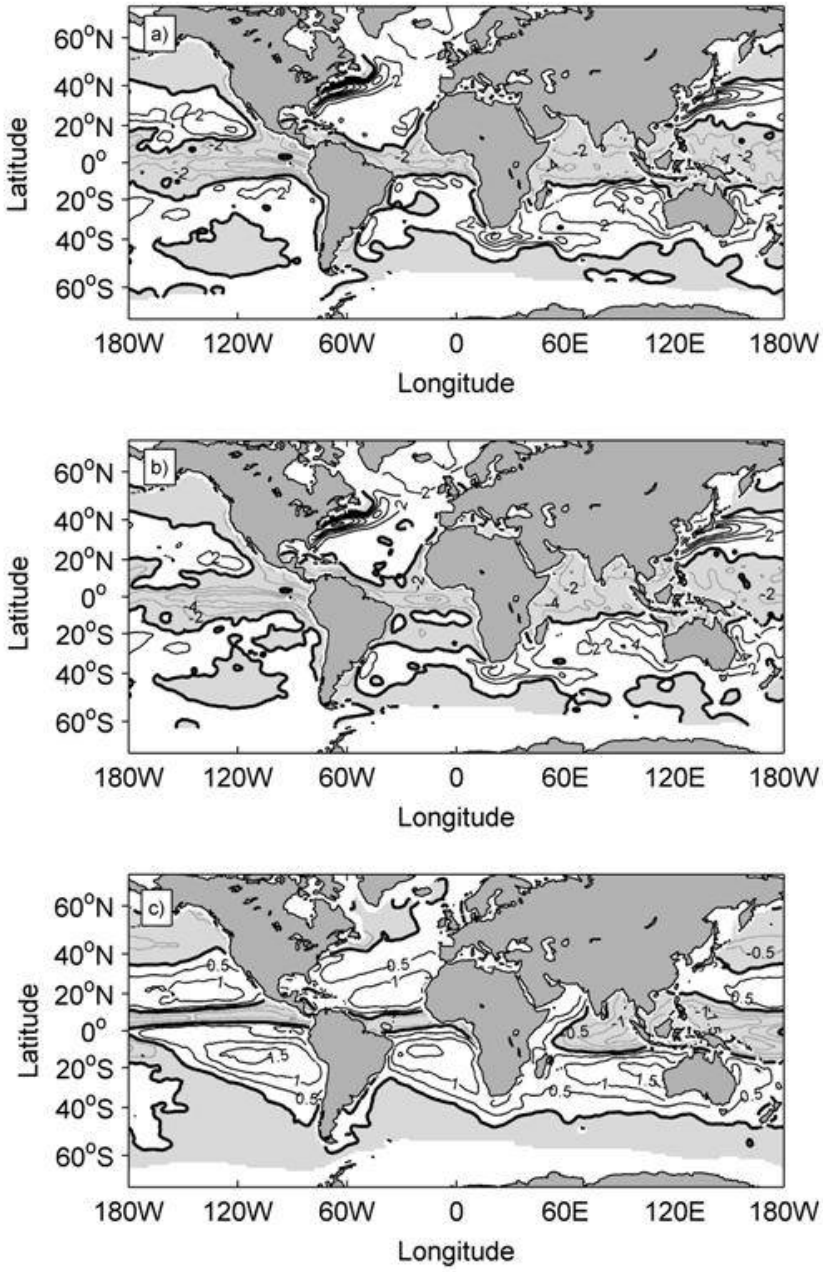

Figure 5 (a) Annual average global surface density flux, D_{IN} with contour intervals of 2mg m^{-2} s^{-1}, positive values thin black line, negative values are shaded. (b) Annual average global thermal contribution to surface density flux, Q_{IN} with contour interval 2mg m^{-2} s^{-1}. (c) Annual average global haline contribution to surface density flux, H_{IN} with contour interval 0.5mg m^3 s^{-1}.

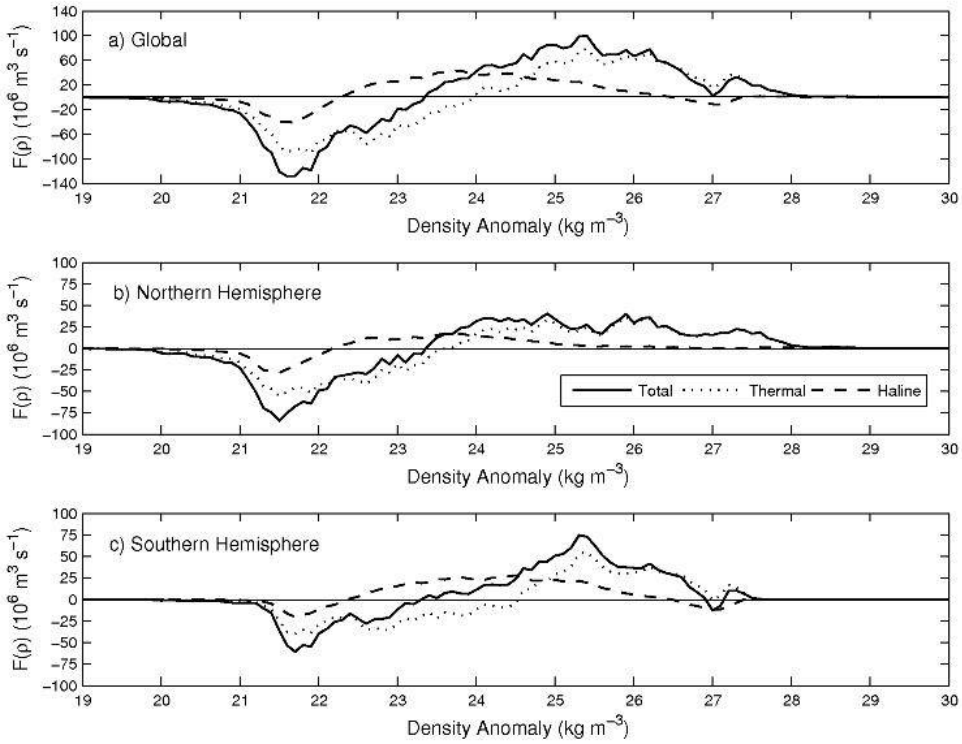

Figure 6 (a) Global annual surface water mass transformation as a function of sea surface density divided into total transformation (solid line), thermal contribution (dotted line) and haline contribution (dashed line). (b) Northern Hemisphere. (c) Southern Hemisphere.

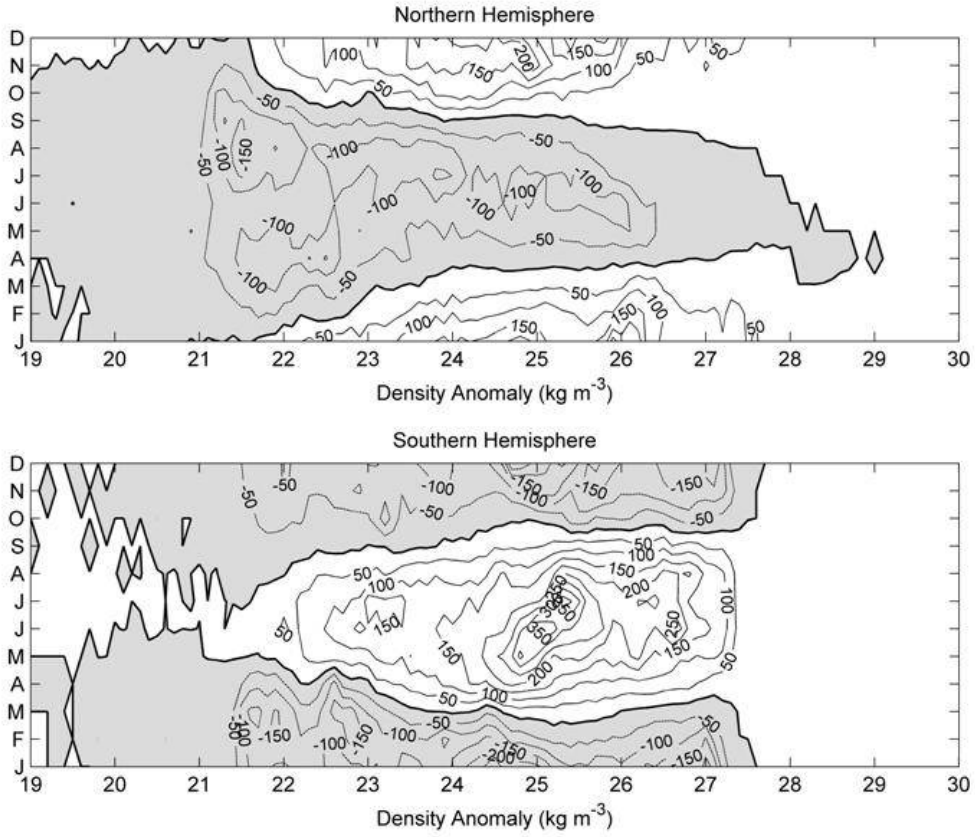

Figure 7 Northern/Southern Hemisphere monthly transformation rate, contour interval 50×10^6 m^3 s^{-1}, thick solid line is contour of zero transformation, negative values are shaded.

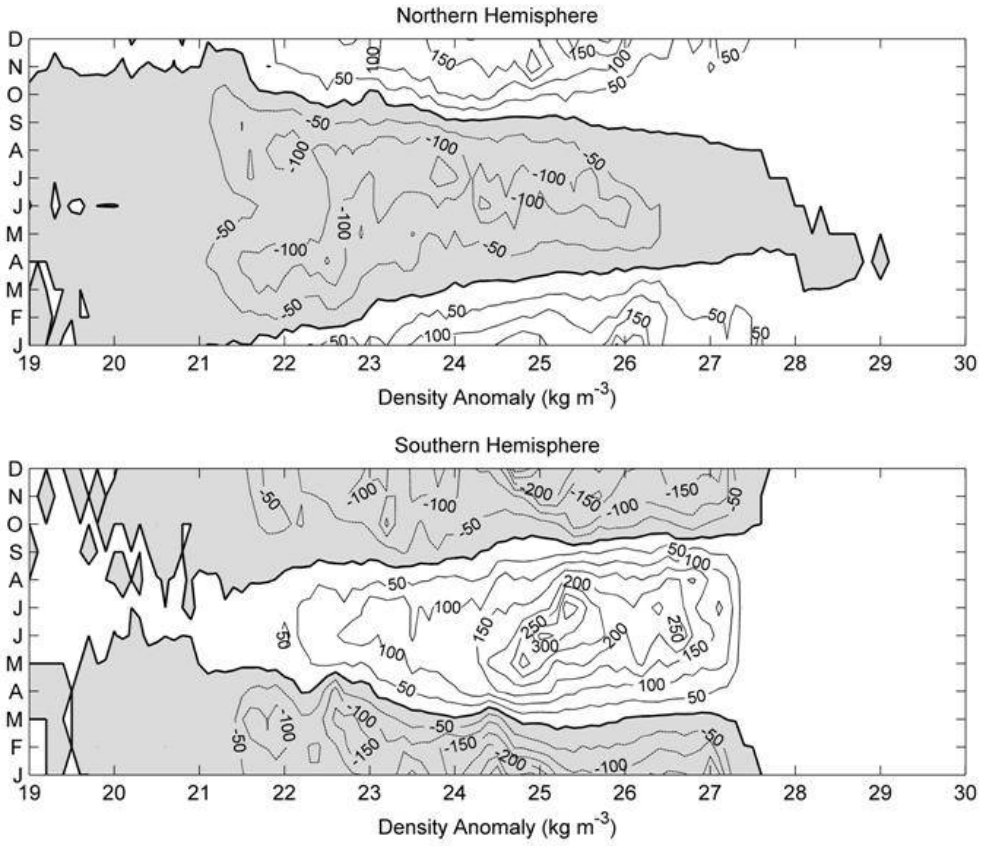

Figure 8 Northern/Southern Hemisphere monthly thermal transformation rate, contour interval 50×10^6 m^3 s^{-1}, thick solid line is contour of zero transformation, negative values are shaded.

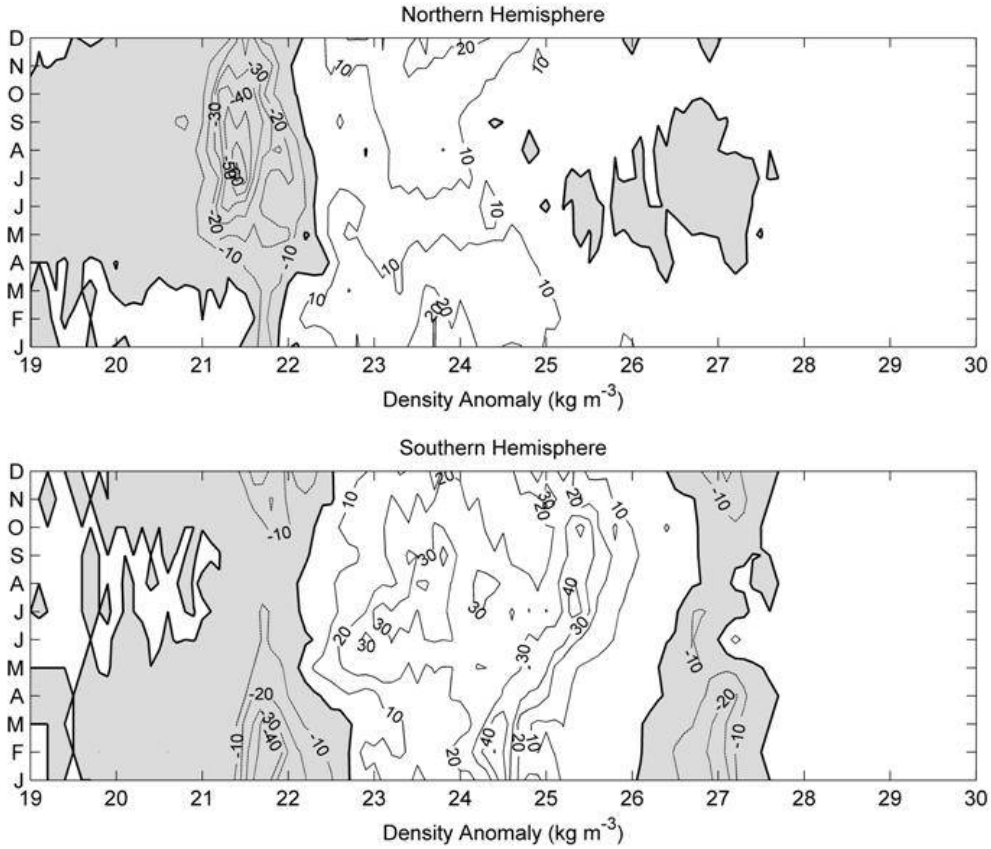

Figure 9 Northern/Southern Hemisphere monthly haline transformation rate, contour interval 10×10^6 m^3 s^{-1}, thick solid line is contour of zero transformation, negative values are shaded.

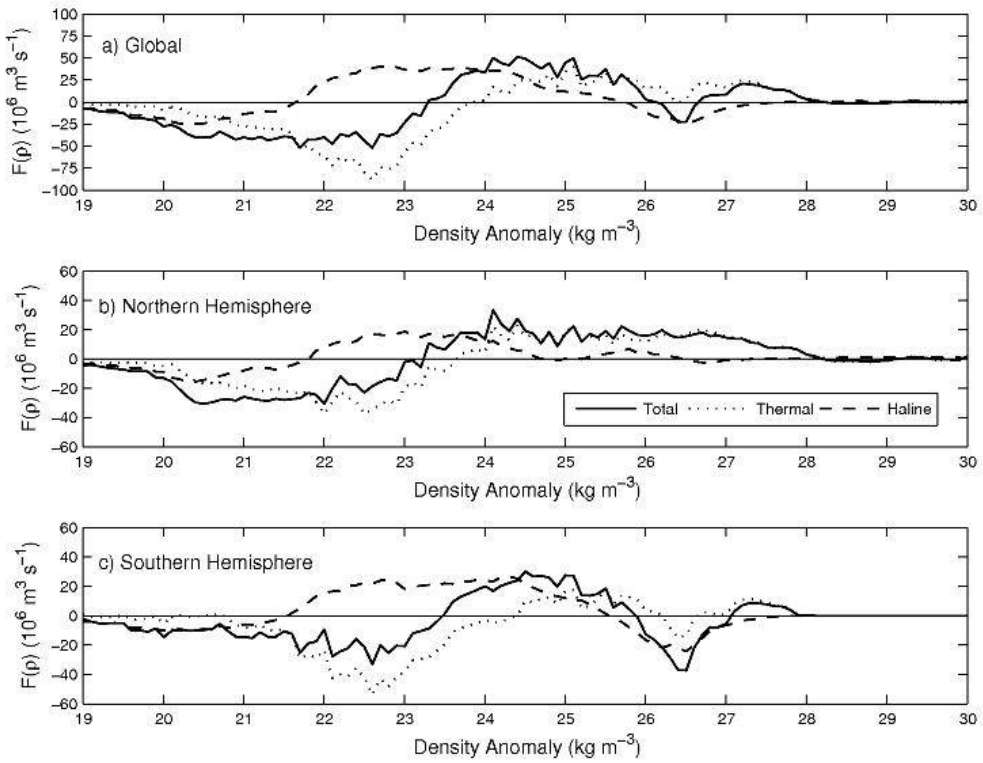

Figure 10 (a) HadCM3 control run global annual surface water mass transformation as a function of sea surface density divided into total transformation, solid line, thermal contribution, dotted line and haline contribution, dashed line. (b) Northern Hemisphere. (c) Southern Hemisphere.

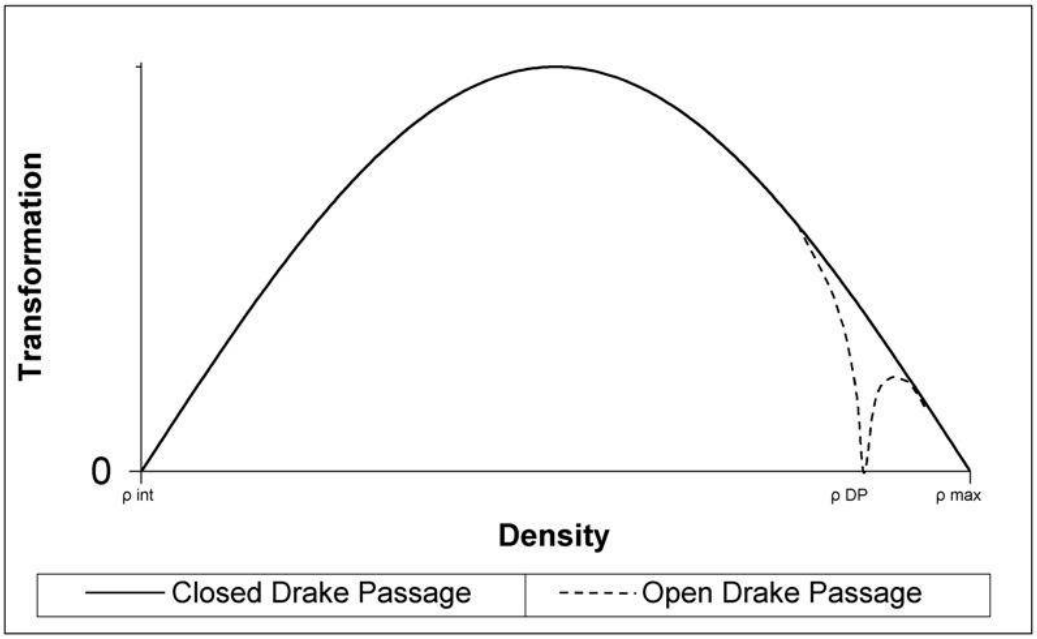

Figure 11 Schematic of transformation curves over a range of densities from intermediate (ρ_{int}) to maximum (ρ_{max}), for an idealised steady state ocean with Drake Passage closed (solid line) and with Drake Passage open (dashed line), where ρ_{DP} is the density class with the outcropping isopycnal which circumnavigates the Southern Ocean uninterrupted by land.